Supporting Online Material for

PAMELA Measurements of Cosmic-Ray Proton and Helium Spectra

O. Adriani, G. C. Barbarino, G. A. Bazilevskaya, R. Bellotti, M. Boezio, E. A. Bogomolov, L. Bonechi, M. Bongi, V. Bonvicini, S. Borisov, S. Bottai, A. Bruno, F. Cafagna, D. Campana, R. Carbone, P. Carlson, M. Casolino, G. Castellini, L. Consiglio, M. P. De Pascale, C. De Santis, N. De Simone, V. Di Felice, A. M. Galper, W. Gillard, L. Grishantseva, G. Jerse, A. V. Karelin, S. V. Koldashov, S. Y. Krutkov, A. N. Kvashnin, A. Leonov, V. Malakhov, V. Malvezzi, L. Marcelli, A. G. Mayorov, W. Menn, V. V. Mikhailov, E. Mocchiutti, A. Monaco, N. Mori, N. Nikonov, G. Osteria, F. Palma, P. Papini, M. Pearce, P. Picozza,* C. Pizzolotto, M. Ricci, S. B. Ricciarini, L. Rossetto, R. Sarkar, M. Simon, R. Sparvoli, P. Spillantini, Y. I. Stozhkov, A. Vacchi, E. Vannuccini, G. Vasilyev, S. A. Voronov, Y. T. Yurkin, J. Wu, G. Zampa, N. Zampa, V. G. Zverev

*To whom correspondence should be addressed. E-mail: picozza@roma2.infn.it

Published 3 March 2011 on *Science* Express
DOI: 10.1126/science.1199172

This PDF file includes:

1 PAMELA Detector

PAMELA consists of several redundant particle detectors capable of providing charge, mass, rigidity and velocity measurements over a wide energy range (Figure S2). The instrument core is a permanent magnet with a silicon microstrip tracker and a scintillator system to provide trigger, charge and time–of–flight information. A silicon-tungsten calorimeter is used for hadron/lepton separation. A shower tail catcher and a neutron detector at the bottom of the apparatus enhance the separation performance. An anticounter system is used to reject background events during the analysis phase. The system is enclosed in a pressurized container (Figure S3) located on one side of the Resurs-DK satellite. The total weight of PAMELA is 470 kg and the power consumption is 355 W.

1.1 Resurs-DK1 Satellite

The Resurs-DK1 satellite (Figure S3) was developed by TsSKB Progress. The spacecraft is three-axis stabilized, with an axis orientation accuracy 0.2 arcmin and an angular velocity stabilization accuracy of 0.005°/s. The spacecraft has a mass of approximately 6650 kg, a height of 7.4 m and a solar array span of 14 m. It is designed to provide imagery of the Earth surface for civilian use. The on-board memory capacity is 769 Gbit. The X-band communications for the payload data permit a downlink data rate of 75 - 300 Mbit/s. Data are sent to ground and processed at the NTsOMZ station in Moscow. The PAMELA data volume amounts to approximately 16 Gbyte/day.

1.2 Scintillator / Time–of–Flight System

The scintillator system provides the experimental trigger and time–of–flight (TOF) information for particles traversing the apparatus. There are three scintillators layers, each composed of two orthogonal planes divided into paddles (8 for S11, 6 for S12, 2 for S21 and S12 and 3 for S32 and S33). There are 6 planes in total and 48 phototubes (each paddle is read by two phototubes). The S1 and S3 (S2) paddles are 7 (5) mm thick. The S1-S3 separation is 77.3 cm. The scintillator system is capable of providing charge information up to $Z = 8$.

1.3 Magnetic Spectrometer

The magnetic spectrometer is built around a permanent magnet which is composed of 5 blocks of segmented Nd-Fe-B alloy with a residual magnetization of 1.3 T. The 12 segments in each block are arranged to provide an almost uniform magnetic field. The size of the magnetic cavity is $13.1 \times 16.1 \times 44.5\ cm^3$, with a mean magnetic field of 0.43 T. Six layers of $300\mu\ m$ thick double-sided microstrip silicon detectors are used to measure particle deflection with $3.0 \pm 0.1\ \mu m$ and $11.5 \pm 0.6\ \mu m$ precision (measured with beam tests and flight data) in the bending and non-bending views, respectively. Each silicon layer comprises three sections which contain two $5.33 \times 7.00\ cm^2$ silicon sensors coupled to a VA1 front-end hybrid circuit.

1.4 Silicon Tungsten Calorimeter

The silicon tungsten sampling calorimeter provides topological and energetic information for particles which generate showers in the calorimeter, allowing lepton/hadron discrimination (*1*) and precise measurement of the energy of impinging electrons and positrons (*2*). The calorimeter comprises 44 single-sided silicon planes (made of nine 380 μm thick, 8$\times$8 cm^2 wide sensors) interleaved with 22 plates of tungsten absorbers, for a total depth of 16.3 X_0 (0.6 nuclear interaction lengths). The silicon sensors are segmented into 32 read-out strips with a 2.4 mm pitch.

The sensors are arranged in a 3×3 matrix and each of the 32 strips is bonded to the corresponding strip on the other two detectors in the same row (or column), hence forming a single 24 cm long read-out strip. The orientation of the strips of two consecutive layers is orthogonal providing two-dimensional spatial information. The CR1.4P ASIC chip (*3*) is used in the front-end electronics, providing a dynamic range of 1400 mips (minimum ionizing particles) and allowing nuclear identification up to Z=26.

1.5 Shower Tail Scintillator

This scintillator ($48 \times 48 \times 1\ cm^3$) is located below the calorimeter and is used to improve hadron/lepton discrimination by measuring the energy not contained in the calorimeter. It can also function as a stand-alone trigger for the neutron detector.

1.6 Neutron Detector

The $60 \times 55 \times 15\ cm^3$ neutron detector is composed of 36 ^3He tubes arranged in two layers and surrounded by polyethylene shielding and a 'U' shaped cadmium layer to remove thermal neutrons not coming from the calorimeter. It is used to improve lepton/hadron identification by detecting the number of neutrons produced in the hadronic and electromagnetic cascades. Hadronic interactions have a much higher neutron production cross section than electromagnetic interactions, where neutrons are primarily produced through nuclear photofission.

1.7 Anticoincidence System

To reject spurious triggers due to particles interacting with the body of the satellite, PAMELA is shielded by plastic anticoincidence scintillators. The CARD anticoincidence system comprises four 8 mm thick scintillators which bound the volume between S1 and S2. The CAT scintillator is placed on top of the magnet and has a central rectangular aperture corresponding to the magnet cavity. This large scintillator is read out by 8 phototubes for redundancy. Four scintillators,

arranged around the magnet, form the CAS lateral anticoincidence system.

2 Detector Characteristics

2.1 Geometrical Factor

The geometrical factor (G_f) of PAMELA was evaluated by defining a fiducial area $0.7\ cm$ from the walls of the $13.1 \times 16.1\ cm^2$ wide magnetic cavity. Only particles passing through this fiducial area were selected for analysis. This definition of fiducial area takes into account the spatial resolution of the calorimeter when extrapolating particle trajectories back into the spectrometer. In this way it was possible to evaluate the tracking efficiency with flight data using particles which cross the calorimeter. The fiducial volume ensures that all particles entering the magnetic cavity can cross the trigger scintillators without impinging on the magnet walls. The derived value of $G_f = 14.55\ cm^2 sr$ was found to be constant above 1 GV within 0.1%. This value has been estimated with a numerical calculation, and was cross-checked with a Monte Carlo simulation. These two values of G_f agree within 0.1%.

2.2 Trigger System

In low radiation regions (close to the geomagnetic equator and outside the South Atlantic Anomaly) the trigger is defined by coincidences between at least one of the two planes of the three scintillator systems ($S1$, $S2$, $S3$). In high latitude regions or inside the radiation belts, the particle rate is higher and dominated by low energy particles. This affects mostly $S1$, and so this plane was excluded from the trigger condition for high-radiation environments. Moreover, a coincidence of all TOF layers of $S2$, $S3$ was required in order to further reduce the trigger rate.

2.3 Live Time

The live time t_{live} of the apparatus was evaluated using the trigger system. Counters for the live and dead time (t_{live}, t_{dead}) were cross-checked with the on-board time of the CPU allowing the acquisition time ($t_{acq} = t_{live} + t_{dead}$) to be determined. Live time errors are negligible compared to other sources of systematic errors.

3 Event Selection

3.1 Contribution of Secondary Particles - The Top of the Payload Correction

Protons and helium nuclei may be lost due to scattering and/or hadronic interactions in the $2\ mm$ thick aluminium pressurized container in which PAMELA is housed or at the top of the apparatus (see Figure S3). Conversely, secondary protons produced in the top of the payload may enter the acceptance window of PAMELA.

In order to estimate the residual contamination of secondary particles a Monte Carlo simulation of protons and helium nuclei impinging on the PAMELA pressurized container was performed. Two different hadronic interactions packages, based respectively on Fluka (*4*) and Geant 4 (*5*), were employed to simulate these interactions.

The dominant contribution to the background was due to secondary singly-charge particles (mostly pions). This background decreases with energy and amounts to less than 1% of the proton flux at 1 GV. Flux attenuation was estimated with simulation and it is constant above several GV. The resulting correction factor accounts for non-elastic interactions and for the loss (gain) of particles from (within) the acceptance due to elastic scattering. The correction factor amounts to $\simeq 6\%$ for protons and $\simeq 12\%$ for helium due to their differing cross-sections.

3.2 Trigger Selection

In this analysis we selected events that did not produce secondary particles in the $S1$ and $S2$ scintillators or the spectrometer. A single track fitted within the spectrometer fiducial acceptance was required, as well as a maximum of one hit paddle matching the extrapolated trajectory in $S1$ and $S2$.

Timing information from the TOF scintillator paddles was used to evaluate the β of the particle. Albedo particles crossing PAMELA from bottom to top were discarded by requiring a positive β.

Particles interacting in the satellite can produce showers which may produce random coincidences in the scintillators of the TOF and anticoincidence systems. Such events were rejected with the TOF selections and by requiring no activity in the CARD and CAT anticoincidence systems. Information from the CAS anticoincidence was not used since these scintillators can be affected by secondaries back-scattered from the calorimeter. The probability for such particles to hit the CARD and CAT systems is significantly lower. This has been studied using experimental data and cross-checked with Monte Carlo simulations. The efficiency of this requirement was included in the flux estimation.

3.3 Proton and Helium Identification

The energy loss of a charged particle traversing matter is described by the Bethe-Bloch equation, $dE/dx \propto Z^2/\beta^2$ (neglecting logarithmic terms). A measurement of the average energy released in the spectrometer planes for a given event at a given rigidity can therefore be used to distinguish between different particles. Proton and helium candidates were selected requiring energy loss in the spectrometer planes compatible with Z=1 and Z=2 nuclei, thereby rejecting positrons, pions and particles with $Z \geq 2$ as shown in Figure S4. The uppermost band is due to helium nuclei which have energy loss in the spectrometer which is four times that experienced

by protons, which occupy the central band. The lesser energy losses below 1 GV are due to positrons, which remain relativistic at low rigidities, and background pions and secondary particles. The black line shows the energy dependent conditions used to select the proton sample. The deuterium component at low rigidities can also be identified in this figure as a band corresponding to larger deposited energy because of the lower β for a given rigidity due to the double atomic number A of deuterium. In this work, no attempt was made to separate D (about 1% of the p flux) and ^{3}He (about 10% of the He flux) isotopes.

3.4 Geomagnetic Selection

The primary (solar and galactic) component needs to be separated from the re-entrant albedo component (particles produced in cosmic ray interactions with the atmosphere below the cutoff and propagating along Earth's magnetic field line). The local geomagnetic cutoff G was evaluated using the Störmer approximation (*6*). A value of $G = 14.9/L^2$ - valid for vertically incident particles - was estimated using the IGRF magnetic field model along the orbit; from this the McIlwain L shell was calculated (*7*). Particles were selected requiring $R > 1.3\,G$ to remove any effect due to directionality in the detector and Earth's penumbral regions. The resulting spectrum was cross-checked with that obtained using only data collected in the polar regions, where the geomagnetic cutoff is below the minimum energy detectable by PAMELA. The two fluxes were found in agreement to better than 1%.

3.5 Tracker Selection

Track Fitting

Particle rigidity was obtained from the fit of the track in the spectrometer. Only events with a single track fully contained inside the fiducial acceptance were selected. For each particle, the tracking system provided up to 12 position measurements (6 in the bending view), which

were interpolated to form a trajectory described by integrating the equations of motion in the magnetic field. An event was selected if the fit of the track had a good χ^2, with an energy dependent selection tuned on experimental data in order to obtain a constant efficiency of 95%. This resulted in a higher χ^2 at low energies due to larger multiple scattering effects.

The Maximum Detectable Rigidity (MDR) for a given detector is defined as the rigidity for which the relative error on the rigidity $\Delta R/R = 100\%$. The momentum resolution and MDR of the magnetic spectrometer depend on the spatial resolution in the bending view and on the topology of the event. For each event the track fitting procedure determines the particle deflection $\eta = \pm 1/R$ and includes a calculation of the parameter covariance matrix. The error associated to the measured deflection η is used as an estimate of the MDR for each event. For in-flight data the values of the MDR thus calculated varied from 200 GV to 1.5 TV, depending on the lever arm and number of hit planes in the bending view and on the incidence angle of the track. The presented results were obtained using events for which the measured rigidity was smaller than the estimated MDR (hence: $R < MDR$). We also derived spectra with different conditions on the rigidity and MDR such as the maximum lever arm, hence $MDR > 1$ TV, obtaining results fully consistent (within the statistical uncertainties) with the presented data.

Spectra were unfolded using a standard procedure and the associated systematic uncertainties have been estimated (Section 4 of the SOM). This procedure relied on a simulation of the apparatus, which for the spectrometer accounted for the measured noise of each silicon plane and performance variations over the duration of the measurement. The simulation code was validated by comparing the distributions of several significant variables (e.g. coordinate residuals, chi-squared and the covariance matrix from the track fitting) with those obtained from real data. This approach was also used in the estimation of the proton-spillover contamination in the antiproton signal (*8*).

Tracker Efficiency

The tracker efficiency was measured by selecting a sample of events which were classified as non-interacting minimum-ionizing particles by the calorimeter. Since the energy of these particles could not be estimated in the calorimeter, the efficiency obtained was an average over all the particles that cross PAMELA. This efficiency was cross-checked with Monte Carlo simulations, showing an agreement to better than 2%.

The overall efficiency of the various selections was evaluated for each energy bin E_i and was found to exceed 75% at a few GV, decreasing gradually to $\simeq 70\%$ for protons and $\simeq 50\%$ for He at 400 GV. The various selection efficiencies were cross checked in each energy bin using the simulation. The error associated to the selection accounted for both statistical ($< 1\%$) and systematic effects.

Tracking-system Uncertainties

The alignment of the spectrometer silicon planes is an important ingredient for this analysis. Misalignment of the tracking sensors has been corrected for by the standard method of track residual minimization. An iterative procedure was employed, which made use of protons, electrons and positrons. The relative positions of the tracking sensors (incoherent alignment) were accurately determined due to the available large statistics of protons. The energy of electrons and positrons could be measured independently with the calorimeter, and so these particles were used to correct for global distortions of the tracking system (coherent alignment), which would mimic a track curvature and result in a deflection offset. A systematic positive shift in deflection would result in an overestimation (underestimation) of the rigidity for electrons (positrons). This issue was quantified by comparing the deflection with the energy measured by the calorimeter. The residual systematic error on the measured deflection could therefore be estimated from the rigidity-to-energy ratio for electrons and positrons. The upper panel of Figure S5 shows the normalized distributions of the ratio P_{trak}/E_{cal} between the momentum measured by the spectrometer and the energy determined with the calorimeter for a flight sam-

ple of electrons (black) and positrons (red), after the alignment correction. A Kolmogorov test of the two distributions gives a probability of 0.85. The bottom panel shows, as an example, the same quantity with an artificially introduced shift of $10^{-3}\,GV^{-1}$ in the spectrometer deflection; the displacement between the electron and the positron distributions is evident in this case. The alignment procedure is sensitive - using Kolmogorov tests at 1-sigma level - down to a deflection offset $|\Delta\eta| \sim 10^{-4}\,GV^{-1}$. This systematic effect was accounted for as an additional uncertainty on the measured spectra and represented the dominant contribution to the total systematic error above 200 GV (see Figure S6). The systematic error on the measured spectra was conservatively evaluated by assuming a 2-standard deviation error in deflection.

It is worth noticing that by using both negatively charged electrons and positively charged positrons, the accuracy of the determination of the deflection offset depends mostly on the positron statistics and only loosely on the energy resolution of the calorimeter.

4 Spectrum Deconvolution

The normalized rigidity distributions of selected protons and helium nuclei were corrected for the effects of rigidity displacement due to finite spectrometer resolution. For events with a rigidity close to the MDR this effect is not negligible and can result in wrongly assigned particle momentum. In the case of a power law spectrum there are more particles with lower rigidity which are wrongly assigned a higher rigidity than vice-versa. Therefore, higher rigidity bins end up with more events, resulting in a harder spectrum expressed as a lower power law index.

As a first approximation the convolution matrix could be considered symmetrical in deflection space, with a spread due to the finite resolution of the tracker. In our case we used Monte Carlo simulations to estimate the detector response matrices for protons and helium. The simulation took into account both physical effects, such as ionization and multiple scattering, and instrumental effects, such as the intrinsic spatial resolution and the alignment uncertainty of

the spectrometer silicon sensors. The estimation of the correlation matrix and the unfolding procedure were performed using a Bayesian approach (*9*).

Two possible systematic effects were considered: the uncertainty associated to the simulated response matrix and the intrinsic accuracy of the adopted unfolding technique. The former was constrained by the matching between measured and simulated spatial residuals and was found to be negligible. The latter was estimated by folding and unfolding a known spectral shape with the spectrometer response and was found to be less than 2%.

5 Statistical Analysis

In this work we employed the statistical procedure based on Fisher's (*10*) and t-Student's tests (*11*) to compare different angular coefficients of two straight lines. The aim of the analysis was to verify or reject the hypothesis of a change of the slope in proton and helium fluxes. Then, as final comparison we performed an alternative analysis using the cumulative sum test (*12*).

5.1 Statistical procedure

We divided each spectrum in two parts:

1. Set1 ($80\ GV \leq R < R_{th}$);
2. Set2 ($R_{th} \leq R \leq 1000$ GV);

with R_{th} ranging between 200 GV and 300 GV. Set1 and Set2 have been fitted with two power laws, and two different spectral indexes ($\gamma 1$ and $\gamma 2$) have been estimated.

We evaluated the variances S_1^2 and S_2^2 of Set1 and Set2 respectively, and from these the Fisher ratio defined as:

$$F = \frac{S_1^2}{S_2^2}, \tag{1}$$

at α-level confidence interval:

$$F_{(1-\frac{\alpha}{2});(n_1-2;n_2-2)} < F < F_{(\frac{\alpha}{2});(n_1-2;n_2-2)}, \tag{2}$$

where $F_{(1-\frac{\alpha}{2});(n_1-2;n_2-2)}$ and $F_{(\frac{\alpha}{2});(n_1-2;n_2-2)}$ are tabulated. If the inequality in (2) hold, the variances S_1^2 and S_2^2 are then statistically consistent. Two different procedures are then followed to compare the fits:

1. If the variances are statistically consistent

2. If the variances are not statistically consistent

5.2 Comparison between two fits when the variances of the data samples are statistically consistent

In this case the experimental value of the two spectral indexes γ_1 and γ_2 are compared according to the following relation:

$$|\gamma_1 - \gamma_2| < t_{\alpha/2}(n_1 + n_2 - 4)S\sqrt{\frac{1}{n_1 S_{1x}^2} + \frac{1}{n_2 S_{2x}^2}}, \tag{3}$$

where:

$t_{\alpha/2}(n_1 + n_2 - 4)$ has been evaluated by means of the t-Student distribution;

$$S^2 = \frac{(n_1 - 2)S_1^2 + (n_2 - 2)S_2^2}{n_1 + n_2 - 4} \tag{4}$$

is the compound variance; S_{1x}^2 and S_{2x}^2 are the variances of the independent variables (rigidity in this case).

For a given α, if (3) is not obeyed, $\gamma_1 \neq \gamma_2$ at $(1 - \alpha)\%$ of confidence level. Otherwise if (3) is obeyed $\gamma_1 = \gamma_2 = \gamma$.

5.3 Comparison between two fits when the variances of the data samples are not statistically consistent

If the variances of the selected data samples are not statistically consistent γ_1 and γ_2 are compared according to the following relation:

$$|\gamma_1 - \gamma_2| < t_{\alpha/2}(\nu) S \sqrt{\frac{S_1^2}{n_1 S_{1x}^2} + \frac{S_2^2}{n_2 S_{2x}^2}}, \tag{5}$$

where

$$\nu = \frac{1}{\frac{A^2}{n_1 - 2} + \frac{1 - A^2}{n_2 - 2}} \tag{6}$$

represents the degrees of freedom of the problem and

$$A = \frac{S_1^2}{n_1 S_{1x}^2} \frac{1}{\frac{S_1^2}{n_1 S_{1x}^2} + \frac{S_2^2}{n_2 S_{2x}^2}}. \tag{7}$$

If (5) is not obeyed, $\gamma_1 \neq \gamma_2$ at $(1 - \alpha)\%$ of confidence level. Otherwise if (5) is obeyed $\gamma_1 = \gamma_2 = \gamma$.

5.4 CUSUM test

As alternative procedure to detect a change of slope in the proton and helium nuclei spectra, we employed a combination of the cumulative sum (CUSUM) test, which computes a cumulative sum of the residuals on data-set (*12*), and bootstrapping method (*13*).

Firstly, we fitted both proton and helium energy spectra, between 80 GV and 1000 GV, with a power law and we computed the residuals η for each flux point:

$$\eta_i = F_i - y_i, \tag{8}$$

where y_i was the experimental value of the flux and F_i was the corresponding value of the fit. The residuals η_i are independent and identically distributed variables, with mean μ and variance

σ^2. The null hypothesis of the test was that a single power law was the best fit of the data-set. Then, the cumulative sum of i_{th} residual, given $S_0 = 0$, is:

$$S_i = S_{i-1}\frac{1}{\sigma}(\mu - \eta_i). \tag{9}$$

The most probable change-point of the data set is the minimum (maximum) of the distribution of the cumulative sums of residuals.

A confidence level for the change can be determined by performing a bootstrap analysis. As estimator of the magnitude of the change we chose S_d, defined by:

$$S_d = S_{max} - S_{min}, \tag{10}$$

with S_{max} and S_{min} the maximum and minimum value of S respectively. The bootstrap analysis consisted of:

1. Performing M numbers of bootstraps re-sampling (re-sampling without replacement) of the data-set.

2. Repeating the procedure of CUSUM test for each bootstrap re-sampling.

3. Computing S_{dj} for each M re-sampling.

4. Counting the number of bootstraps re-sampling K for which $S_d < S_{dj}$.

Then, the confidence level that a change occurred was :

$$C.L. = 100\frac{K}{M}\%. \tag{11}$$

Applying a bootstrap procedure with M = 10^6 re-sampling to the CUSUM test, we obtained that the single power law hypothesis was rejected at 99.9% and at 96.2% confidence level in the rigidity range 80-1000 GV for the proton and helium data, respectively.

6 Spectral Indexes

6.1 Spectral Indexes in Kinetic Energy

Given a cosmic ray spectrum Φ_R described by a rigidity (R) power law:

$$\Phi_R = \frac{dN}{dR} = \Phi_0 R^{-\gamma}, \tag{12}$$

the corresponding spectrum Φ_T in total kinetic energy T is given by

$$\Phi_T = \frac{dN}{dT} = \frac{dN}{dR}\frac{dR}{dT}, \tag{13}$$

with:

$$R = \frac{1}{Z}\sqrt{T^2 + 2Tmc^2}, \tag{14}$$

$$\frac{dR}{dT} = \frac{1}{Z}\frac{T + mc^2}{\sqrt{T^2 + 2Tmc^2}}, \tag{15}$$

for a particle of charge Z and mass m. Therefore

$$\Phi_T = \Phi_0 Z^{\gamma-1}(T^2 + 2Tmc^2)^{-\gamma/2}\frac{T + mc^2}{\sqrt{T^2 + 2Tmc^2}}. \tag{16}$$

The spectral index γ_R is given by:

$$\gamma_R = -\frac{dlog(\Phi_R)}{dlog(R)} \tag{17}$$

and the corresponding spectral index in kinetic energy γ_T is:

$$\gamma_T = -\frac{dlog(\phi_T)}{logT} = (\gamma_R + 1)\frac{T^2 + Tmc^2}{T^2 + 2Tmc^2} - \frac{T}{T + mc^2}. \tag{18}$$

The difference between γ_T and γ_R is about 10% at 30 GV and 1% at 100 GV, so that performing the fit in kinetic energy yields a different value of γ according to the interval it is performed. If we express PAMELA data in kinetic energy per nucleon we obtain from the fit: $\gamma^T_{30-1000\ GeV,p} = 2.782 \pm 0.003(stat) \pm 0.004(syst)$ and $\gamma^T_{15-600\ GeV/n,he} = 2.712 \pm 0.01(stat) \pm 0.007(syst)$, in agreement with the results in rigidity and equation 18.

6.2 Rigidity Dependent Spectral Index

To quantify and parametrize the concavity in the 30-230 GV range it is possible to fit the data with a law of the form:

$$\Phi = A * R^{-\Gamma} = A * R^{-\gamma - \alpha \frac{R-R_0}{R_0}}, \tag{19}$$

the next order approximation in the Taylor expansion of the function describing the particle flux, with α representing the amount of deviation from the single power law. The resulting values are (with $R_0 = 100GV$) $\Gamma_p = \gamma_p + \alpha \frac{R-R_0}{R_0}$, with $\gamma_p = 2.790 \pm 0.008 \pm 0.001$ and $\alpha_p = (1.07 \pm 0.25 \pm 0.05) \cdot 10^{-2}$.

In the helium spectrum, we have $\Gamma_{he} = \gamma_{he} + \alpha_{he} \frac{R-R_0}{R_0}$, with $\gamma_{he} = 2.691 \pm 0.015 \pm 0.003$ and $\alpha_{he} = (1.2 \pm 0.2 \pm 0.1) \cdot 10^{-2}$.

Under this parametrization the value of the spectral index $\gamma_R(R)$ can be used to compare the data with previous measurements:

$$\gamma_R(R) = \frac{dlog(\Phi_R)}{dlog(R)} = \gamma_0 - \alpha(1 - \frac{R}{R_0}(logR + 1)). \tag{20}$$

The resulting curves are shown in Figure 4 of the main text.

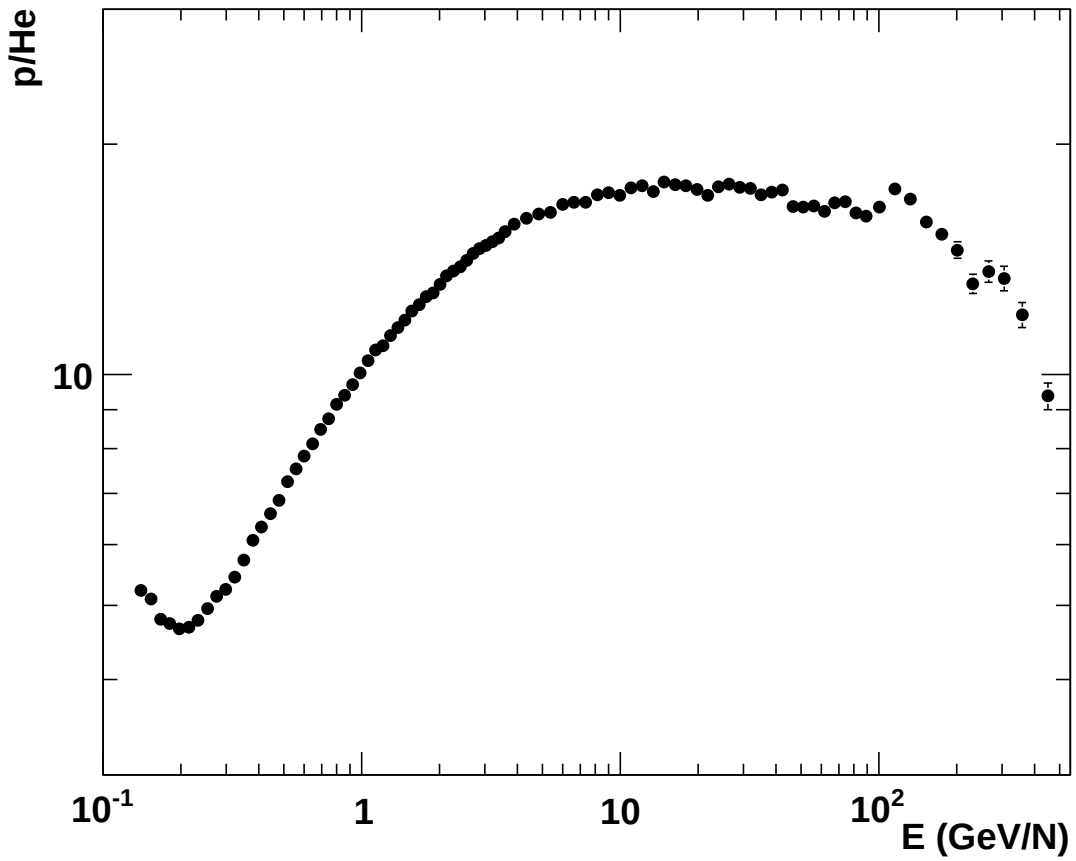

Figure S1: Proton and helium ratio vs kinetic energy per nucleon. It is possible to see that the energy behavior of the spectrum is not as regular as the ratio expressed as function of the rigidity.

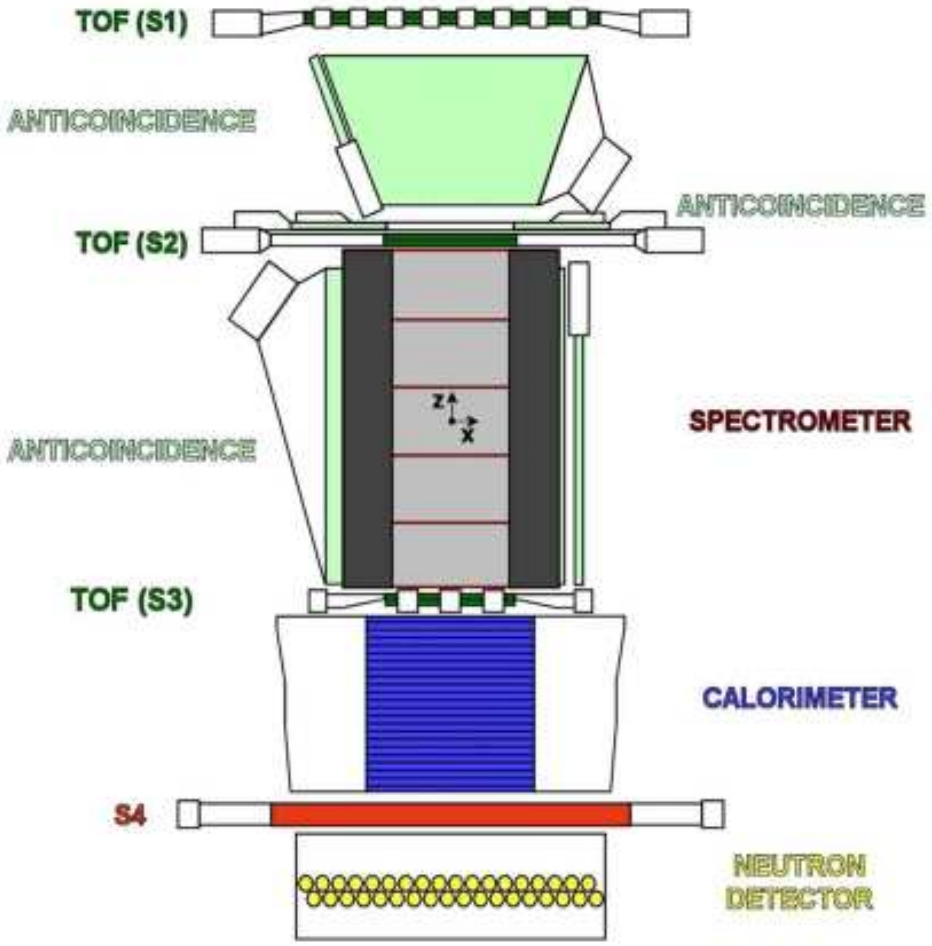

Figure S2: Scheme of the detectors composing PAMELA. S1, S2, S3, S4: scintillator planes.

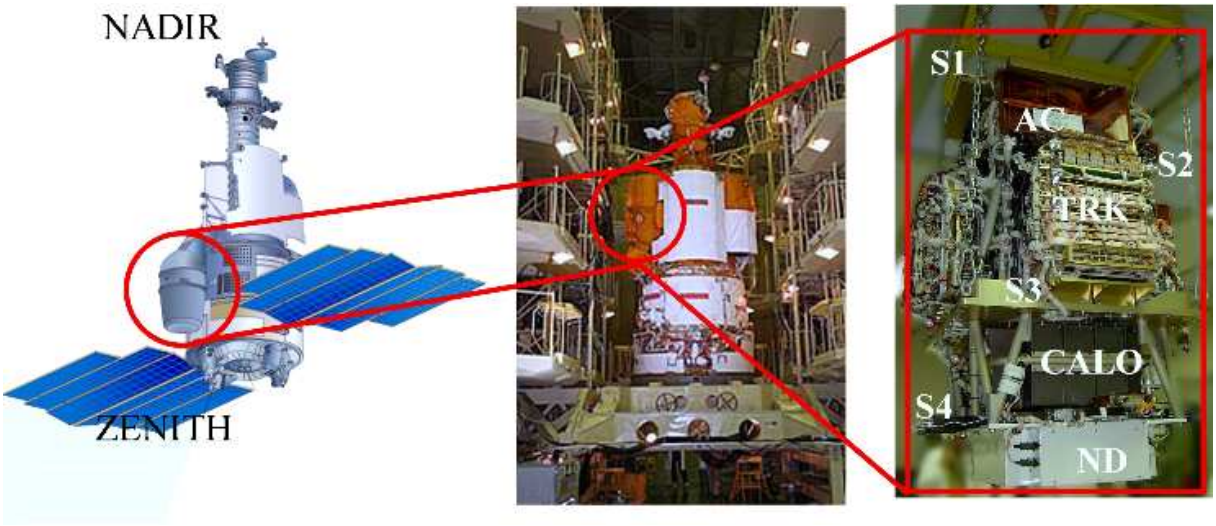

Figure S3: Left: Scheme of the Resurs-DK1 satellite. PAMELA is located in the pressurized container on the left of the picture. In the scheme the pressurized container is in the acquisition configuration. Center: The Resurs-DK1 satellite during integration in Samara. The pressurized container housing PAMELA is in the folded (launch) position. Right: Photo of the PAMELA detector during integration in Tor Vergata with marked the position of the detectors. S1, S2, S3, S4: scintillator planes; AC: top anticoincidence; TRK: tracker core; CALO: Silicon-Tungsten calorimeter; ND: Neutron Detector.

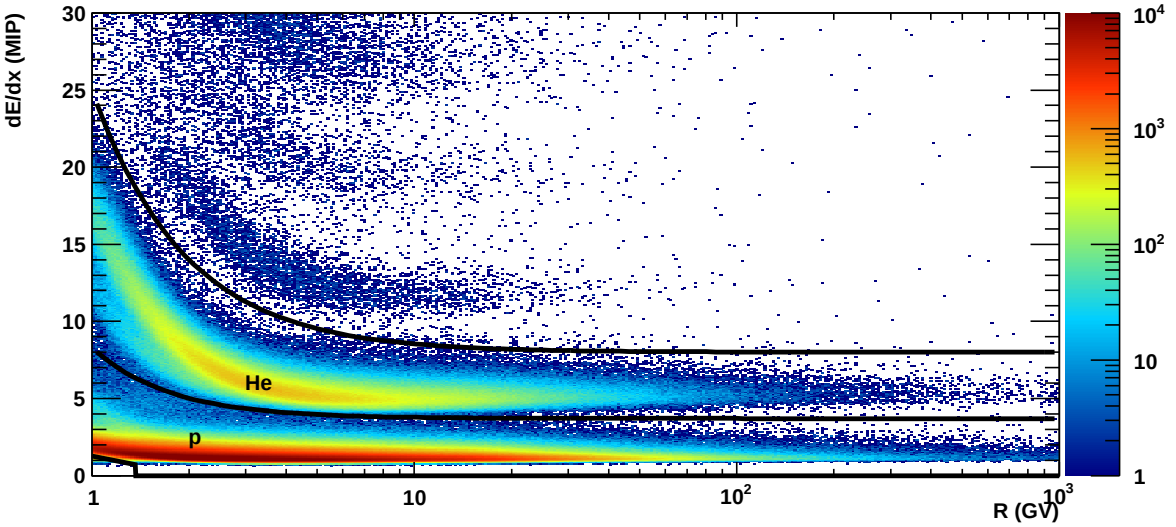

Figure S4: Energy loss in tracker (mean in all planes hit) vs tracker rigidity for positively charged particles. The lines represent the selections used to select protons and He nuclei. Higher bands are due to heavier nuclei.

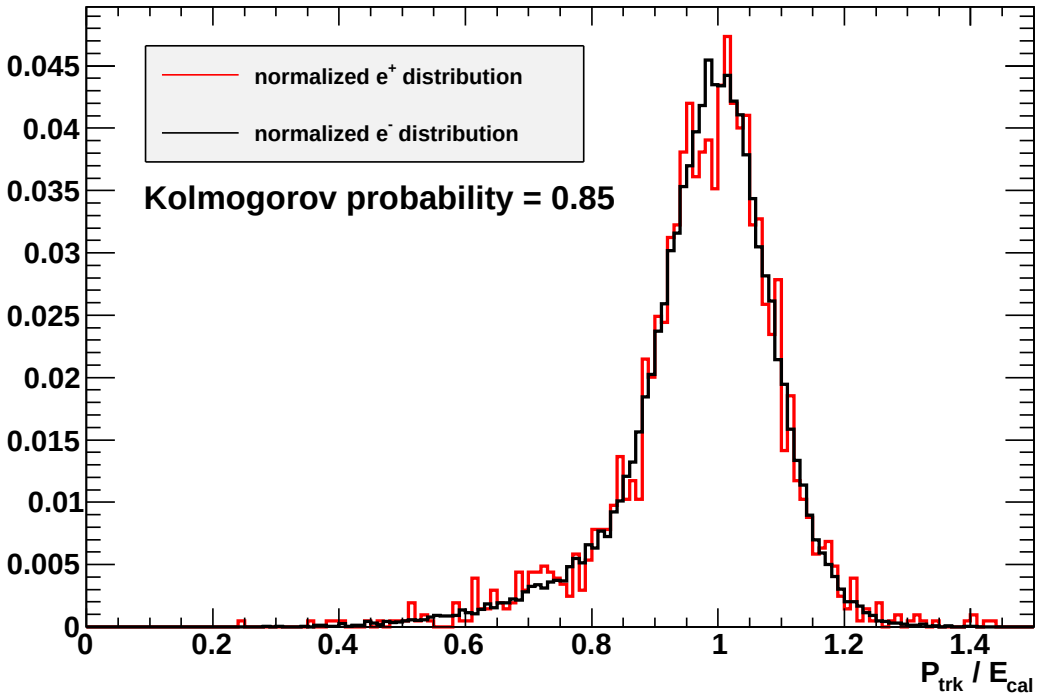

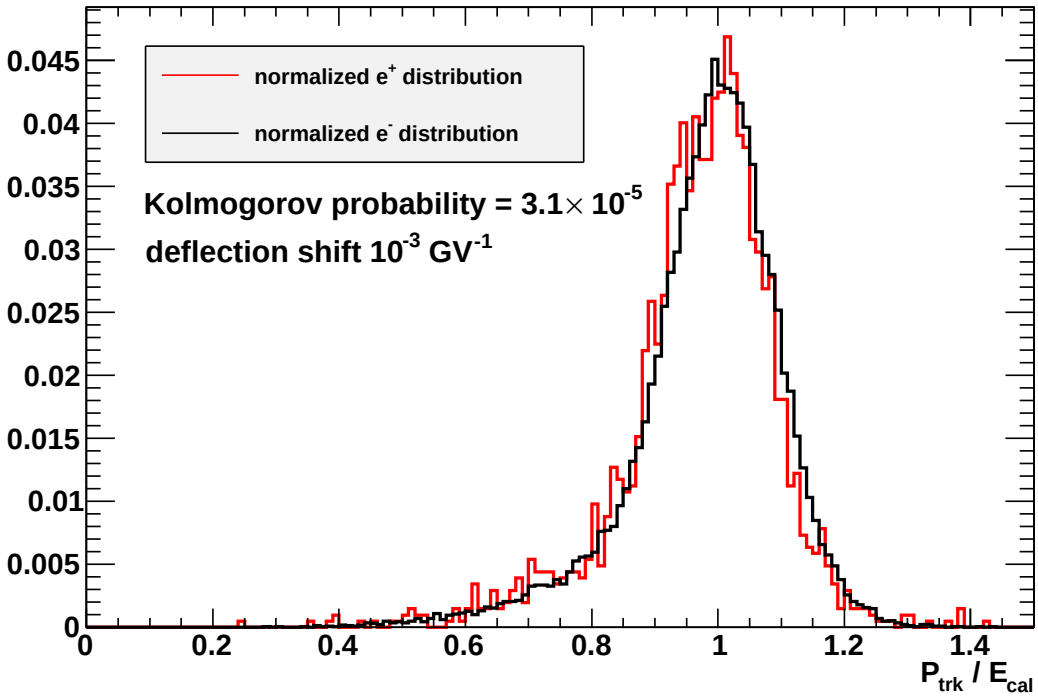

Figure S5: Upper panel: Normalized distributions of the ratio $r = P_{trk}/E_{cal}$ between the momentum measured by the spectrometer and the energy determined with the calorimeter for a flight sample of electrons (black) and positrons (red). The two distributions are in agreement (Kolmogorov test) with p=0.85. Bottom panel: The same quantity r with an artificial shift of $10^{-3}\ GV^{-1}$ to the spectrometer deflection; the displacement between the electron and the positron distributions is evident. The alignment procedure is sensitive – using Kolmogorov tests at 1-sigma level – up to a deflection offset $|\Delta\eta| \sim 10^{-4} GV^{-1}$.

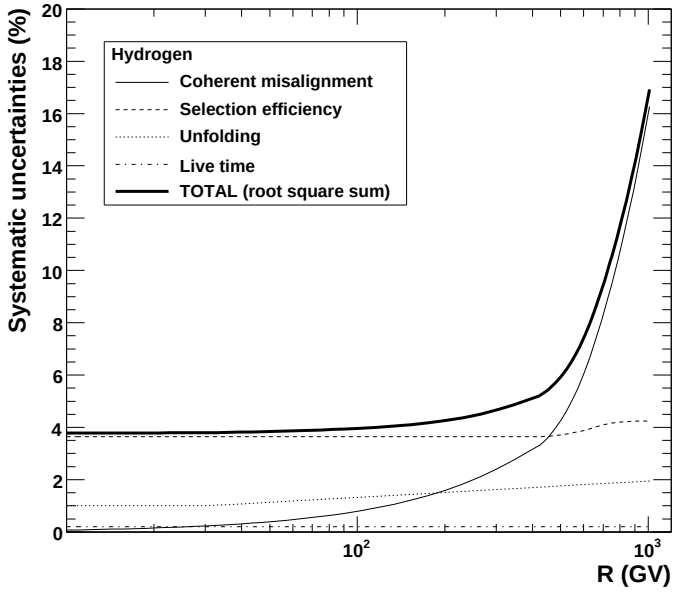

Figure S6: Estimated systematic uncertainties to the measured proton and helium fluxes.

Nuclei injection index below / above break rigidity	Break rigidity (GV)	Diffusion coefficient		Alfvén speed v_A Km/s
		value at $\rho = 3$ GV (cm^2 s^{-1})	index	
1.82/2.36	4	$5.2 \cdot 10^{28}$	0.34	36

Table S1: GALPROP parameters for the reacceleration model of (*14*), used in Figures 2 and 3 of the main text.

	Particle	Class I	Class II	Class III
Zatsepin model	proton	$1.4 \cdot 10^4$	$6.25 \cdot 10^3$	0.6
(original)	helium	$8.5 \cdot 10^3$	$8.5 \cdot 10^3$	1.5
Zatsepin model	proton	$(7.1 \pm 0.1) \cdot 10^3$	$6.25 \cdot 10^3$ (fixed)	3.0 ± 0.05
(fitted to data)	helium	$(9.5 \pm 1.8) \cdot 10^3$	$8.5 \cdot 10^3$ (fixed)	0.74 ± 0.04

Table S2: Parameters of the multi-source model of (*15*), used in Figures 2 and 3 of the main text.

Protons

Kinetic Energy Interval (GeV)	Mean Kinetic Energy (GeV)	H Flux $\pm$ stat $\pm$ sys $(m^2\,sr\,s\,GeV)^{-1}$
0.43 - 0.46	0.44	$1581 \pm 3 \pm 60$
0.46 - 0.50	0.48	$1549 \pm 3 \pm 60$
0.50 - 0.54	0.52	$1527 \pm 3 \pm 60$
0.54 - 0.58	0.56	$1484 \pm 3 \pm 60$
0.58 - 0.62	0.60	$1444 \pm 2 \pm 60$
0.62 - 0.67	0.65	$1402 \pm 2 \pm 50$
0.67 - 0.72	0.70	$1349 \pm 2 \pm 50$
0.72 - 0.77	0.75	$1293 \pm 2 \pm 50$
0.77 - 0.83	0.80	$1233 \pm 2 \pm 50$
0.83 - 0.89	0.86	$1171 \pm 2 \pm 40$
0.89 - 0.96	0.92	$1113 \pm 2 \pm 40$
0.96 - 1.02	0.99	$1053 \pm 2 \pm 40$
1.02 - 1.09	1.06	$996 \pm 1 \pm 40$
1.09 - 1.17	1.13	$933 \pm 1 \pm 40$
1.17 - 1.25	1.21	$871 \pm 1 \pm 30$
1.25 - 1.33	1.29	$813 \pm 1 \pm 30$
1.33 - 1.42	1.38	$758 \pm 1 \pm 30$
1.42 - 1.52	1.47	$703 \pm 1 \pm 30$
1.52 - 1.62	1.57	$652.6 \pm 0.9 \pm 30$
1.62 - 1.72	1.67	$601.8 \pm 0.8 \pm 20$
1.72 - 1.83	1.78	$555.5 \pm 0.8 \pm 20$
1.83 - 1.95	1.89	$510.0 \pm 0.7 \pm 20$
1.95 - 2.07	2.01	$472.0 \pm 0.7 \pm 20$
2.07 - 2.20	2.13	$434.3 \pm 0.6 \pm 20$
2.20 - 2.33	2.27	$396.5 \pm 0.6 \pm 20$
2.33 - 2.47	2.40	$362.4 \pm 0.5 \pm 10$
2.47 - 2.62	2.55	$331.5 \pm 0.5 \pm 10$
2.62 - 2.78	2.70	$303.2 \pm 0.4 \pm 10$
2.78 - 2.94	2.86	$276.0 \pm 0.4 \pm 10$
2.94 - 3.12	3.03	$250.2 \pm 0.4 \pm 9$
3.12 - 3.30	3.21	$227.0 \pm 0.4 \pm 9$
3.30 - 3.49	3.39	$205.8 \pm 0.3 \pm 8$
3.49 - 3.69	3.59	$187.2 \pm 0.3 \pm 7$
3.69 - 4.12	3.90	$160.7 \pm 0.2 \pm 6$
4.12 - 4.59	4.35	$130.2 \pm 0.2 \pm 5$
4.59 - 5.11	4.84	$105.3 \pm 0.1 \pm 4$
5.11 - 5.68	5.38	$84.8 \pm 0.1 \pm 3$
5.68 - 6.30	5.98	$68.0 \pm 0.1 \pm 3$

6.30 - 6.99	6.64	$54.48 \pm 0.08 \pm 2$
6.99 - 7.74	7.36	$43.33 \pm 0.07 \pm 2$
7.74 - 8.57	8.15	$34.40 \pm 0.06 \pm 1$
8.57 - 9.48	9.01	$27.28 \pm 0.05 \pm 1$
9.48 - 10.48	9.97	$21.62 \pm 0.04 \pm 0.8$
10.48 - 11.57	11.01	$17.00 \pm 0.03 \pm 0.6$
11.57 - 12.77	12.16	$13.35 \pm 0.03 \pm 0.5$
12.77 - 14.09	13.41	$10.51 \pm 0.02 \pm 0.4$
14.09 - 15.54	14.79	$8.28 \pm 0.02 \pm 0.3$
15.54 - 17.12	16.31	$6.47 \pm 0.02 \pm 0.3$
17.12 - 18.86	17.96	$5.01 \pm 0.01 \pm 0.2$
18.86 - 20.76	19.78	$3.90 \pm 0.01 \pm 0.2$
20.76 - 22.85	21.78	$3.050 \pm 0.009 \pm 0.1$
22.85 - 25.15	23.97	$2.367 \pm 0.007 \pm 0.09$
25.15 - 27.66	26.37	$1.828 \pm 0.006 \pm 0.07$
27.66 - 30.42	29.00	$1.420 \pm 0.005 \pm 0.05$
30.42 - 33.44	31.88	$1.107 \pm 0.004 \pm 0.04$
33.44 - 36.75	35.05	$(849 \pm 4 \pm 30) \times 10^{-3}$
36.75 - 40.39	38.52	$(653 \pm 3 \pm 30) \times 10^{-3}$
40.39 - 44.37	42.32	$(509 \pm 3 \pm 20) \times 10^{-3}$
44.37 - 48.74	46.49	$(397 \pm 2 \pm 20) \times 10^{-3}$
48.74 - 53.53	51.07	$(301 \pm 2 \pm 10) \times 10^{-3}$
53.53 - 58.79	56.08	$(233 \pm 2 \pm 9) \times 10^{-3}$
58.79 - 64.55	61.58	$(178 \pm 1 \pm 7) \times 10^{-3}$
64.55 - 70.86	67.61	$(141 \pm 1 \pm 5) \times 10^{-3}$
70.86 - 77.79	74.22	$(110.3 \pm 0.9 \pm 4) \times 10^{-3}$
77.79 - 85.38	81.47	$(83.1 \pm 0.8 \pm 3) \times 10^{-3}$
85.38 - 93.71	89.42	$(63.3 \pm 0.6 \pm 3) \times 10^{-3}$
93.71 - 107.73	100.41	$(45.9 \pm 0.4 \pm 2) \times 10^{-3}$
107.73 - 123.83	115.42	$(31.2 \pm 0.3 \pm 1) \times 10^{-3}$
123.83 - 142.31	132.66	$(20.9 \pm 0.3 \pm 0.8) \times 10^{-3}$
142.31 - 163.54	152.46	$(14.2 \pm 0.2 \pm 0.6) \times 10^{-3}$
163.54 - 187.90	175.18	$(9.5 \pm 0.2 \pm 0.4) \times 10^{-3}$
187.90 - 215.88	201.27	$(6.4 \pm 0.1 \pm 0.3) \times 10^{-3}$
215.88 - 248.00	231.23	$(4.17 \pm 0.08 \pm 0.2) \times 10^{-3}$
248.00 - 284.88	265.62	$(2.97 \pm 0.07 \pm 0.1) \times 10^{-3}$
284.88 - 327.23	305.12	$(2.02 \pm 0.05 \pm 0.09) \times 10^{-3}$
327.23 - 393.60	358.45	$(1.32 \pm 0.03 \pm 0.06) \times 10^{-3}$
393.60 - 519.17	450.82	$(0.68 \pm 0.02 \pm 0.04) \times 10^{-3}$
519.17 - 653.84	581.52	$(0.38 \pm 0.02 \pm 0.03) \times 10^{-3}$
653.84 - 862.22	748.78	$(0.19 \pm 0.01 \pm 0.02) \times 10^{-3}$

862.22 - 1190.55	1009.40	$(0.081 \pm 0.007 \pm 0.01) \times 10^{-3}$

Table S3: Flux measurement for protons in kinetic energy.

Helium

Kinetic Energy Interval (GeV/n)	Mean Kinetic Energy (GeV/n)	He Flux $\pm$ stat $\pm$ sys $(m^2\ sr\ s\ (GeV/n))^{-1}$
0.12 - 0.13	0.13	$179 \pm 2 \pm 7$
0.13 - 0.15	0.14	$217 \pm 2 \pm 8$
0.15 - 0.16	0.15	$249 \pm 2 \pm 9$
0.16 - 0.17	0.17	$281 \pm 2 \pm 10$
0.17 - 0.19	0.18	$300 \pm 2 \pm 10$
0.19 - 0.20	0.20	$315 \pm 2 \pm 10$
0.20 - 0.22	0.21	$320 \pm 2 \pm 10$
0.22 - 0.24	0.23	$322 \pm 1 \pm 10$
0.24 - 0.26	0.25	$316 \pm 1 \pm 10$
0.26 - 0.29	0.27	$308 \pm 1 \pm 10$
0.29 - 0.31	0.30	$302 \pm 1 \pm 10$
0.31 - 0.34	0.32	$291 \pm 1 \pm 10$
0.34 - 0.36	0.35	$278 \pm 1 \pm 10$
0.36 - 0.39	0.38	$264 \pm 1 \pm 10$
0.39 - 0.42	0.41	$252.9 \pm 0.9 \pm 9$
0.42 - 0.46	0.44	$241.7 \pm 0.8 \pm 9$
0.46 - 0.50	0.47	$227.4 \pm 0.8 \pm 9$
0.50 - 0.53	0.51	$212.0 \pm 0.7 \pm 8$
0.53 - 0.58	0.55	$198.1 \pm 0.7 \pm 7$
0.58 - 0.62	0.60	$185.6 \pm 0.6 \pm 7$
0.62 - 0.67	0.64	$173.7 \pm 0.6 \pm 7$
0.67 - 0.72	0.69	$160.1 \pm 0.5 \pm 6$
0.72 - 0.77	0.74	$148.8 \pm 0.5 \pm 6$
0.77 - 0.83	0.80	$135.5 \pm 0.4 \pm 5$
0.83 - 0.89	0.85	$125.4 \pm 0.4 \pm 5$
0.89 - 0.95	0.92	$115.4 \pm 0.4 \pm 4$
0.95 - 1.02	0.98	$105.4 \pm 0.3 \pm 4$
1.02 - 1.09	1.05	$96.2 \pm 0.3 \pm 4$
1.09 - 1.17	1.12	$87.1 \pm 0.3 \pm 3$
1.17 - 1.25	1.20	$80.3 \pm 0.3 \pm 3$
1.25 - 1.33	1.28	$72.7 \pm 0.3 \pm 3$
1.33 - 1.42	1.37	$66.2 \pm 0.2 \pm 3$
1.42 - 1.51	1.46	$60.0 \pm 0.2 \pm 2$
1.51 - 1.61	1.56	$54.2 \pm 0.2 \pm 2$
1.61 - 1.72	1.66	$49.1 \pm 0.2 \pm 2$
1.72 - 1.83	1.77	$44.2 \pm 0.2 \pm 2$
1.83 - 2.06	1.94	$38.3 \pm 0.1 \pm 1$

2.06 - 2.33	2.19	$30.80 \pm 0.09 \pm 1$
2.33 - 2.62	2.46	$25.03 \pm 0.07 \pm 0.9$
2.62 - 2.94	2.77	$20.08 \pm 0.06 \pm 0.8$
2.94 - 3.29	3.10	$16.18 \pm 0.05 \pm 0.6$
3.29 - 3.68	3.47	$13.02 \pm 0.04 \pm 0.5$
3.68 - 4.10	3.88	$10.29 \pm 0.04 \pm 0.4$
4.10 - 4.57	4.33	$8.19 \pm 0.03 \pm 0.3$
4.57 - 5.09	4.82	$6.54 \pm 0.03 \pm 0.2$
5.09 - 5.66	5.36	$5.24 \pm 0.02 \pm 0.2$
5.66 - 6.28	5.96	$4.10 \pm 0.02 \pm 0.2$
6.28 - 6.97	6.61	$3.26 \pm 0.01 \pm 0.1$
6.97 - 7.72	7.33	$2.60 \pm 0.01 \pm 0.1$
7.72 - 8.55	8.12	$2.016 \pm 0.009 \pm 0.08$
8.55 - 9.46	8.98	$1.588 \pm 0.008 \pm 0.06$
9.46 - 10.45	9.93	$1.270 \pm 0.007 \pm 0.05$
10.45 - 11.54	10.98	$(976 \pm 6 \pm 40) \times 10^{-3}$
11.54 - 12.74	12.12	$(762 \pm 5 \pm 30) \times 10^{-3}$
12.74 - 14.05	13.37	$(610 \pm 4 \pm 20) \times 10^{-3}$
14.05 - 15.50	14.75	$(466 \pm 3 \pm 20) \times 10^{-3}$
15.50 - 17.08	16.26	$(368 \pm 3 \pm 10) \times 10^{-3}$
17.08 - 18.81	17.91	$(286 \pm 2 \pm 10) \times 10^{-3}$
18.81 - 20.71	19.73	$(225 \pm 2 \pm 9) \times 10^{-3}$
20.71 - 22.80	21.72	$(179 \pm 2 \pm 7) \times 10^{-3}$
22.80 - 25.08	23.90	$(136 \pm 2 \pm 5) \times 10^{-3}$
25.08 - 27.59	26.29	$(104 \pm 1 \pm 4) \times 10^{-3}$
27.59 - 30.34	28.92	$(81 \pm 1 \pm 3) \times 10^{-3}$
30.34 - 33.36	31.80	$(63.7 \pm 0.9 \pm 2) \times 10^{-3}$
33.36 - 36.66	34.95	$(49.9 \pm 0.7 \pm 2) \times 10^{-3}$
36.66 - 40.29	38.42	$(38.0 \pm 0.6 \pm 2) \times 10^{-3}$
40.29 - 44.26	42.21	$(29.4 \pm 0.5 \pm 1) \times 10^{-3}$
44.26 - 48.62	46.37	$(24.1 \pm 0.4 \pm 0.9) \times 10^{-3}$
48.62 - 55.96	52.12	$(17.1 \pm 0.3 \pm 0.7) \times 10^{-3}$
55.96 - 64.39	59.98	$(11.7 \pm 0.2 \pm 0.5) \times 10^{-3}$
64.39 - 74.07	69.01	$(8.0 \pm 0.2 \pm 0.3) \times 10^{-3}$
74.07 - 85.18	79.37	$(5.5 \pm 0.1 \pm 0.2) \times 10^{-3}$
85.18 - 97.94	91.27	$(3.7 \pm 0.1 \pm 0.2) \times 10^{-3}$
97.94 - 112.58	104.93	$(2.42 \pm 0.08 \pm 0.1) \times 10^{-3}$
112.58 - 129.40	120.61	$(1.55 \pm 0.06 \pm 0.07) \times 10^{-3}$
129.40 - 148.71	138.62	$(1.11 \pm 0.05 \pm 0.05) \times 10^{-3}$
148.71 - 170.88	159.30	$(0.81 \pm 0.04 \pm 0.04) \times 10^{-3}$
170.88 - 196.33	183.03	$(0.55 \pm 0.03 \pm 0.03) \times 10^{-3}$

196.33 - 225.56	210.29	$(0.39 \pm 0.02 \pm 0.02) \times 10^{-3}$
225.56 - 259.12	241.59	$(0.29 \pm 0.02 \pm 0.02) \times 10^{-3}$
259.12 - 326.45	290.29	$(0.17 \pm 0.01 \pm 0.01) \times 10^{-3}$
326.45 - 430.64	373.92	$(0.10 \pm 0.01 \pm 0.01) \times 10^{-3}$
430.64 - 594.81	504.23	$(0.06 \pm 0.01 \pm 0.009) \times 10^{-3}$

Table S4: Flux measurement for Helium in kinetic energy per nucleon

Protons

Rigidity (GV/c)	Mean Rigidity (GV/c)	H Flux $\pm$ stat $\pm$ sys $(m^2\ sr\ s\ (GV/c))^{-1}$
0.99 - 1.04	1.01	$1161 \pm 2 \pm 40$
1.04 - 1.09	1.06	$1161 \pm 2 \pm 40$
1.09 - 1.14	1.11	$1167 \pm 2 \pm 40$
1.14 - 1.19	1.16	$1156 \pm 2 \pm 40$
1.19 - 1.25	1.22	$1144 \pm 2 \pm 40$
1.25 - 1.31	1.28	$1130 \pm 2 \pm 40$
1.31 - 1.37	1.34	$1104 \pm 2 \pm 40$
1.37 - 1.43	1.40	$1074 \pm 2 \pm 40$
1.43 - 1.50	1.47	$1038 \pm 2 \pm 40$
1.50 - 1.57	1.54	$999 \pm 1 \pm 40$
1.57 - 1.64	1.61	$961 \pm 1 \pm 40$
1.64 - 1.72	1.68	$919 \pm 1 \pm 40$
1.72 - 1.80	1.76	$879 \pm 1 \pm 30$
1.80 - 1.89	1.85	$832 \pm 1 \pm 30$
1.89 - 1.98	1.93	$783 \pm 1 \pm 30$
1.98 - 2.07	2.02	$738 \pm 1 \pm 30$
2.07 - 2.17	2.12	$692.9 \pm 0.9 \pm 30$
2.17 - 2.27	2.22	$647.2 \pm 0.9 \pm 20$
2.27 - 2.38	2.32	$605.1 \pm 0.8 \pm 20$
2.38 - 2.49	2.43	$561.5 \pm 0.8 \pm 20$
2.49 - 2.61	2.55	$521.3 \pm 0.7 \pm 20$
2.61 - 2.73	2.67	$481.1 \pm 0.7 \pm 20$
2.73 - 2.86	2.79	$447.4 \pm 0.6 \pm 20$
2.86 - 2.99	2.92	$413.5 \pm 0.6 \pm 20$
2.99 - 3.13	3.06	$379.1 \pm 0.5 \pm 10$
3.13 - 3.28	3.21	$347.8 \pm 0.5 \pm 10$
3.28 - 3.44	3.36	$319.3 \pm 0.5 \pm 10$
3.44 - 3.60	3.52	$292.9 \pm 0.4 \pm 10$
3.60 - 3.77	3.68	$267.5 \pm 0.4 \pm 10$
3.77 - 3.95	3.86	$243.1 \pm 0.4 \pm 9$
3.95 - 4.13	4.04	$221.1 \pm 0.3 \pm 8$
4.13 - 4.33	4.23	$200.9 \pm 0.3 \pm 8$
4.33 - 4.53	4.43	$183.2 \pm 0.3 \pm 7$
4.53 - 4.97	4.74	$157.7 \pm 0.2 \pm 6$
4.97 - 5.45	5.20	$128.1 \pm 0.2 \pm 5$
5.45 - 5.97	5.70	$103.9 \pm 0.1 \pm 4$
5.97 - 6.55	6.25	$83.9 \pm 0.1 \pm 3$
6.55 - 7.18	6.86	$67.35 \pm 0.09 \pm 3$

7.18 - 7.87	7.52	$54.06 \pm 0.08 \pm 2$
7.87 - 8.63	8.24	$43.05 \pm 0.07 \pm 2$
8.63 - 9.46	9.04	$34.22 \pm 0.06 \pm 1$
9.46 - 10.38	9.91	$27.16 \pm 0.05 \pm 1$
10.38 - 11.38	10.86	$21.53 \pm 0.04 \pm 0.8$
11.38 - 12.48	11.91	$16.95 \pm 0.03 \pm 0.6$
12.48 - 13.68	13.06	$13.32 \pm 0.03 \pm 0.5$
13.68 - 15.00	14.32	$10.48 \pm 0.02 \pm 0.4$
15.00 - 16.45	15.70	$8.26 \pm 0.02 \pm 0.3$
16.45 - 18.03	17.22	$6.46 \pm 0.02 \pm 0.2$
18.03 - 19.77	18.88	$5.00 \pm 0.01 \pm 0.2$
19.77 - 21.68	20.70	$3.90 \pm 0.01 \pm 0.2$
21.68 - 23.77	22.70	$3.047 \pm 0.009 \pm 0.1$
23.77 - 26.07	24.89	$2.365 \pm 0.007 \pm 0.09$
26.07 - 28.58	27.29	$1.827 \pm 0.006 \pm 0.07$
28.58 - 31.34	29.92	$1.419 \pm 0.005 \pm 0.05$
31.34 - 34.36	32.81	$1.107 \pm 0.004 \pm 0.04$
34.36 - 37.68	35.97	$(849 \pm 4 \pm 30) \times 10^{-3}$
37.68 - 41.31	39.44	$(653 \pm 3 \pm 30) \times 10^{-3}$
41.31 - 45.30	43.25	$(509 \pm 3 \pm 20) \times 10^{-3}$
45.30 - 49.67	47.42	$(397 \pm 2 \pm 20) \times 10^{-3}$
49.67 - 54.46	52.00	$(301 \pm 2 \pm 10) \times 10^{-3}$
54.46 - 59.72	57.01	$(233 \pm 2 \pm 9) \times 10^{-3}$
59.72 - 65.48	62.51	$(178 \pm 1 \pm 7) \times 10^{-3}$
65.48 - 71.79	68.54	$(141 \pm 1 \pm 5) \times 10^{-3}$
71.79 - 78.72	75.16	$(110.3 \pm 0.9 \pm 4) \times 10^{-3}$
78.72 - 86.32	82.41	$(83.1 \pm 0.8 \pm 3) \times 10^{-3}$
86.32 - 94.64	90.36	$(63.3 \pm 0.6 \pm 3) \times 10^{-3}$
94.64 - 108.67	101.34	$(45.9 \pm 0.4 \pm 2) \times 10^{-3}$
108.67 - 124.77	116.36	$(31.2 \pm 0.3 \pm 1) \times 10^{-3}$
124.77 - 143.25	133.60	$(20.9 \pm 0.3 \pm 0.8) \times 10^{-3}$
143.25 - 164.47	153.39	$(14.2 \pm 0.2 \pm 0.6) \times 10^{-3}$
164.47 - 188.84	176.12	$(9.5 \pm 0.2 \pm 0.4) \times 10^{-3}$
188.84 - 216.82	202.21	$(6.4 \pm 0.1 \pm 0.3) \times 10^{-3}$
216.82 - 248.94	232.16	$(4.17 \pm 0.08 \pm 0.2) \times 10^{-3}$
248.94 - 285.82	266.56	$(2.97 \pm 0.07 \pm 0.1) \times 10^{-3}$
285.82 - 328.16	306.05	$(2.02 \pm 0.05 \pm 0.09) \times 10^{-3}$
328.16 - 394.54	359.39	$(1.32 \pm 0.03 \pm 0.06) \times 10^{-3}$
394.54 - 520.11	451.75	$(0.68 \pm 0.02 \pm 0.04) \times 10^{-3}$
520.11 - 654.77	582.46	$(0.38 \pm 0.02 \pm 0.03) \times 10^{-3}$
654.77 - 863.16	749.72	$(0.19 \pm 0.01 \pm 0.02) \times 10^{-3}$

863.16 - 1191.49	1010.34	$(0.081 \pm 0.007 \pm 0.01) \times 10^{-3}$

Table S5: Flux measurement for protons in rigidity.

Helium

Rigidity (GV/c)	Mean Rigidity (GV/c)	He Flux $\pm$ stat $\pm$ sys $(m^2\ sr\ s\ (GV/c))^{-1}$
0.99 - 1.04	1.01	$42.4 \pm 0.4 \pm 2$
1.04 - 1.09	1.06	$53.2 \pm 0.4 \pm 2$
1.09 - 1.14	1.11	$63.4 \pm 0.4 \pm 2$
1.14 - 1.19	1.16	$74.0 \pm 0.4 \pm 3$
1.19 - 1.25	1.22	$81.4 \pm 0.4 \pm 3$
1.25 - 1.31	1.27	$88.4 \pm 0.4 \pm 3$
1.31 - 1.37	1.33	$92.7 \pm 0.4 \pm 3$
1.37 - 1.43	1.40	$96.0 \pm 0.4 \pm 4$
1.43 - 1.50	1.46	$97.1 \pm 0.4 \pm 4$
1.50 - 1.57	1.53	$97.3 \pm 0.4 \pm 4$
1.57 - 1.64	1.60	$98.1 \pm 0.4 \pm 4$
1.64 - 1.72	1.68	$96.9 \pm 0.4 \pm 4$
1.72 - 1.80	1.76	$95.0 \pm 0.4 \pm 4$
1.80 - 1.89	1.84	$92.5 \pm 0.3 \pm 3$
1.89 - 1.98	1.93	$90.6 \pm 0.3 \pm 3$
1.98 - 2.07	2.02	$88.5 \pm 0.3 \pm 3$
2.07 - 2.17	2.11	$85.0 \pm 0.3 \pm 3$
2.17 - 2.27	2.21	$80.8 \pm 0.3 \pm 3$
2.27 - 2.38	2.32	$77.0 \pm 0.3 \pm 3$
2.38 - 2.49	2.43	$73.4 \pm 0.2 \pm 3$
2.49 - 2.61	2.54	$69.9 \pm 0.2 \pm 3$
2.61 - 2.73	2.66	$65.4 \pm 0.2 \pm 3$
2.73 - 2.86	2.79	$61.7 \pm 0.2 \pm 2$
2.86 - 2.99	2.92	$57.0 \pm 0.2 \pm 2$
2.99 - 3.13	3.06	$53.4 \pm 0.2 \pm 2$
3.13 - 3.28	3.20	$49.8 \pm 0.2 \pm 2$
3.28 - 3.44	3.35	$46.0 \pm 0.2 \pm 2$
3.44 - 3.60	3.51	$42.4 \pm 0.1 \pm 2$
3.60 - 3.77	3.67	$38.8 \pm 0.1 \pm 2$
3.77 - 3.95	3.85	$36.1 \pm 0.1 \pm 1$
3.95 - 4.13	4.03	$32.9 \pm 0.1 \pm 1$
4.13 - 4.33	4.22	$30.2 \pm 0.1 \pm 1$
4.33 - 4.53	4.42	$27.6 \pm 0.1 \pm 1$
4.53 - 4.74	4.63	$25.13 \pm 0.09 \pm 0.9$
4.74 - 4.97	4.85	$22.89 \pm 0.08 \pm 0.9$
4.97 - 5.20	5.07	$20.73 \pm 0.08 \pm 0.8$
5.20 - 5.70	5.44	$18.08 \pm 0.05 \pm 0.7$
5.70 - 6.25	5.96	$14.69 \pm 0.04 \pm 0.6$

6.25 - 6.86	6.54	$12.03 \pm 0.03 \pm 0.5$
6.86 - 7.52	7.17	$9.71 \pm 0.03 \pm 0.4$
7.52 - 8.24	7.86	$7.87 \pm 0.03 \pm 0.3$
8.24 - 9.04	8.62	$6.36 \pm 0.02 \pm 0.2$
9.04 - 9.91	9.45	$5.05 \pm 0.02 \pm 0.2$
9.91 - 10.87	10.37	$4.03 \pm 0.02 \pm 0.2$
10.87 - 11.91	11.37	$3.22 \pm 0.01 \pm 0.1$
11.91 - 13.06	12.46	$2.59 \pm 0.01 \pm 0.1$
13.06 - 14.32	13.67	$2.031 \pm 0.008 \pm 0.08$
14.32 - 15.71	14.99	$1.619 \pm 0.007 \pm 0.06$
15.71 - 17.22	16.43	$1.292 \pm 0.006 \pm 0.05$
17.22 - 18.88	18.02	$1.003 \pm 0.005 \pm 0.04$
18.88 - 20.71	19.76	$(790 \pm 4 \pm 30) \times 10^{-3}$
20.71 - 22.70	21.67	$(633 \pm 3 \pm 20) \times 10^{-3}$
22.70 - 24.89	23.76	$(486 \pm 3 \pm 20) \times 10^{-3}$
24.89 - 27.30	26.05	$(380 \pm 2 \pm 10) \times 10^{-3}$
27.30 - 29.93	28.56	$(304 \pm 2 \pm 10) \times 10^{-3}$
29.93 - 32.82	31.32	$(233 \pm 2 \pm 9) \times 10^{-3}$
32.82 - 35.98	34.34	$(184 \pm 1 \pm 7) \times 10^{-3}$
35.98 - 39.45	37.66	$(143 \pm 1 \pm 5) \times 10^{-3}$
39.45 - 43.26	41.29	$(112 \pm 1 \pm 4) \times 10^{-3}$
43.26 - 47.43	45.28	$(89.6 \pm 0.9 \pm 3) \times 10^{-3}$
47.43 - 52.01	49.64	$(67.7 \pm 0.7 \pm 3) \times 10^{-3}$
52.01 - 57.03	54.44	$(51.9 \pm 0.6 \pm 2) \times 10^{-3}$
57.03 - 62.53	59.69	$(40.7 \pm 0.5 \pm 2) \times 10^{-3}$
62.53 - 68.56	65.45	$(31.8 \pm 0.4 \pm 1) \times 10^{-3}$
68.56 - 75.18	71.76	$(24.9 \pm 0.4 \pm 1) \times 10^{-3}$
75.18 - 82.43	78.69	$(19.0 \pm 0.3 \pm 0.7) \times 10^{-3}$
82.43 - 90.38	86.28	$(14.7 \pm 0.3 \pm 0.6) \times 10^{-3}$
90.38 - 99.10	94.60	$(12.1 \pm 0.2 \pm 0.5) \times 10^{-3}$
99.10 - 113.79	106.11	$(8.6 \pm 0.2 \pm 0.3) \times 10^{-3}$
113.79 - 130.65	121.83	$(5.8 \pm 0.1 \pm 0.2) \times 10^{-3}$
130.65 - 150.00	139.88	$(3.98 \pm 0.09 \pm 0.2) \times 10^{-3}$
150.00 - 172.22	160.61	$(2.75 \pm 0.07 \pm 0.1) \times 10^{-3}$
172.22 - 197.74	184.40	$(1.86 \pm 0.05 \pm 0.08) \times 10^{-3}$
197.74 - 227.03	211.72	$(1.21 \pm 0.04 \pm 0.05) \times 10^{-3}$
227.03 - 260.67	243.09	$(0.78 \pm 0.03 \pm 0.03) \times 10^{-3}$
260.67 - 299.29	279.11	$(0.56 \pm 0.02 \pm 0.03) \times 10^{-3}$
299.29 - 343.63	320.46	$(0.41 \pm 0.02 \pm 0.02) \times 10^{-3}$
343.63 - 394.54	367.94	$(0.28 \pm 0.02 \pm 0.01) \times 10^{-3}$
394.54 - 452.99	422.46	$(0.20 \pm 0.01 \pm 0.01) \times 10^{-3}$

452.99 - 520.11	485.05	$(0.14 \pm 0.01 \pm 0.008) \times 10^{-3}$
520.11 - 654.77	582.45	$(0.084 \pm 0.006 \pm 0.006) \times 10^{-3}$
654.77 - 863.16	749.71	$(0.051 \pm 0.005 \pm 0.005) \times 10^{-3}$
863.16 - 1191.49	1010.33	$(0.030 \pm 0.007 \pm 0.005) \times 10^{-3}$

Table S6: Flux measurement for Helium in rigidity.

H/He

Rigidity (GV/c)	H Flux / He Flux
1.01	$27.2 \pm 0.2 \pm 1$
1.06	$21.7 \pm 0.2 \pm 1$
1.11	$18.3 \pm 0.1 \pm 0.8$
1.16	$15.53 \pm 0.09 \pm 0.7$
1.22	$13.98 \pm 0.08 \pm 0.6$
1.28	$12.73 \pm 0.07 \pm 0.6$
1.34	$11.85 \pm 0.06 \pm 0.5$
1.40	$11.14 \pm 0.05 \pm 0.5$
1.47	$10.64 \pm 0.05 \pm 0.5$
1.54	$10.23 \pm 0.04 \pm 0.5$
1.61	$9.76 \pm 0.04 \pm 0.4$
1.68	$9.45 \pm 0.04 \pm 0.4$
1.76	$9.22 \pm 0.04 \pm 0.4$
1.85	$8.96 \pm 0.03 \pm 0.4$
1.93	$8.61 \pm 0.03 \pm 0.4$
2.02	$8.31 \pm 0.03 \pm 0.4$
2.12	$8.12 \pm 0.03 \pm 0.4$
2.22	$7.98 \pm 0.03 \pm 0.4$
2.32	$7.84 \pm 0.03 \pm 0.4$
2.43	$7.63 \pm 0.03 \pm 0.3$
2.55	$7.44 \pm 0.03 \pm 0.3$
2.67	$7.33 \pm 0.03 \pm 0.3$
2.79	$7.23 \pm 0.03 \pm 0.3$
2.92	$7.24 \pm 0.03 \pm 0.3$
3.06	$7.08 \pm 0.03 \pm 0.3$
3.21	$6.97 \pm 0.03 \pm 0.3$
3.36	$6.92 \pm 0.03 \pm 0.3$
3.52	$6.89 \pm 0.03 \pm 0.3$
3.68	$6.88 \pm 0.03 \pm 0.3$
3.86	$6.72 \pm 0.03 \pm 0.3$
4.04	$6.70 \pm 0.03 \pm 0.3$
4.23	$6.63 \pm 0.03 \pm 0.3$
4.43	$6.62 \pm 0.03 \pm 0.3$
4.64	$6.58 \pm 0.03 \pm 0.3$
4.85	$6.54 \pm 0.03 \pm 0.3$
5.08	$6.49 \pm 0.03 \pm 0.3$
5.45	$6.38 \pm 0.02 \pm 0.3$
5.97	$6.34 \pm 0.02 \pm 0.3$

6.55	$6.26 \pm 0.02 \pm 0.3$
7.18	$6.19 \pm 0.02 \pm 0.3$
7.87	$6.13 \pm 0.02 \pm 0.3$
8.63	$6.03 \pm 0.02 \pm 0.3$
9.46	$6.03 \pm 0.02 \pm 0.3$
10.38	$5.99 \pm 0.02 \pm 0.3$
11.38	$5.92 \pm 0.03 \pm 0.3$
12.47	$5.79 \pm 0.03 \pm 0.3$
13.68	$5.81 \pm 0.03 \pm 0.3$
15.00	$5.74 \pm 0.03 \pm 0.3$
16.44	$5.64 \pm 0.03 \pm 0.3$
18.03	$5.63 \pm 0.03 \pm 0.3$
19.77	$5.60 \pm 0.03 \pm 0.3$
21.68	$5.41 \pm 0.03 \pm 0.2$
23.77	$5.52 \pm 0.04 \pm 0.3$
26.06	$5.47 \pm 0.04 \pm 0.3$
28.57	$5.27 \pm 0.04 \pm 0.2$
31.33	$5.40 \pm 0.04 \pm 0.2$
34.35	$5.27 \pm 0.05 \pm 0.2$
37.67	$5.20 \pm 0.05 \pm 0.2$
41.30	$5.12 \pm 0.05 \pm 0.2$
45.29	$4.99 \pm 0.06 \pm 0.2$
49.66	$5.11 \pm 0.06 \pm 0.2$
54.45	$5.09 \pm 0.07 \pm 0.2$
59.70	$5.04 \pm 0.07 \pm 0.2$
65.46	$4.95 \pm 0.08 \pm 0.2$
71.77	$4.96 \pm 0.08 \pm 0.2$
78.70	$5.09 \pm 0.09 \pm 0.2$
86.29	$4.9 \pm 0.1 \pm 0.2$
94.62	$4.6 \pm 0.1 \pm 0.2$
106.12	$4.77 \pm 0.09 \pm 0.2$
121.84	$4.6 \pm 0.1 \pm 0.2$
139.89	$4.7 \pm 0.1 \pm 0.2$
160.62	$4.5 \pm 0.1 \pm 0.2$
184.42	$4.4 \pm 0.1 \pm 0.2$
211.74	$4.5 \pm 0.2 \pm 0.2$
243.11	$4.8 \pm 0.2 \pm 0.2$
279.12	$4.7 \pm 0.2 \pm 0.2$
320.47	$4.6 \pm 0.3 \pm 0.2$
367.95	$4.3 \pm 0.3 \pm 0.2$
422.47	$4.1 \pm 0.3 \pm 0.2$

485.06	$3.9 \pm 0.3 \pm 0.2$
582.46	$4.6 \pm 0.4 \pm 0.2$
749.72	$3.7 \pm 0.5 \pm 0.2$
1010.34	$2.7 \pm 0.7 \pm 0.2$

Table S7: Proton/Helium ratio in rigidity.

References and Notes

1. M. Boezio, *et al.*, *Astroparticle Physics* **26**, 111 (2006).

2. M. Boezio, *et al.*, *Nuclear Instruments and Methods in Physics Research A* **487**, 407 (2002).

3. V. Bonvicini, *Proc. 5th International Workshop on Front-end Electronic "FEE 2003", Snowmass* (http://www-ppd.fnal.gov/EEDOffice-w/conferences/FEE_2003/FEE2003talks/G5_Bonvicini.pdf, 2003).

4. F. Ballarini, *et al.*, *Advances in Space Research* **40**, 1339 (2007).

5. J. Allison, *et al.*, *IEEE Transactions on Nuclear Science* **53**, 270 (2006).

6. M. A. Shea, *et al.*, *Physics of the Earth and Planetary Interiors* **48**, 200 (1987).

7. International geomagnetic reference field, *Tech. rep.*, IAGA (2005).

8. O. Adriani, *et al.*, *Physical Review Letters* **105**, 121101 (2010).

9. D'Agostini, G., *Nuclear Instruments and Methods in Physics Research A* **362**, 487 (1995).

10. R. A. Fisher, *Statistical Methods for Research Workers* (Eighth, London, 1941).

11. A. N. Shiryaev, *Graduate Texts in Mathematics: Probability* (Springer, New York, 1995).

12. R. L. Brown, J. Durbin, J. M. Evans, *Journal of the Royal Statistics Society B* **37**, 149 (1975).

13. C. Z. Mooney, R. D. Duval, *BOOTSTRAPPING: A Nonparametric Approach to Statistical Inference* (Sage University Paper series on Quantitative Applications in the Social Sciences, 07-095. Newbury Park, CA:Sage, 1993).

14. V. S. Ptuskin, I. V. Moskalenko, F. C. Jones, A. W. Strong, V. N. Zirakashvili, *Astrophysical Journal* **642**, 902 (2006).

15. V. I. Zatsepin, N. V. Sokolskaya, *Astron. Astrophys.* **458**, 1 (2006).